Faraday Discussions

Accepted Manuscript

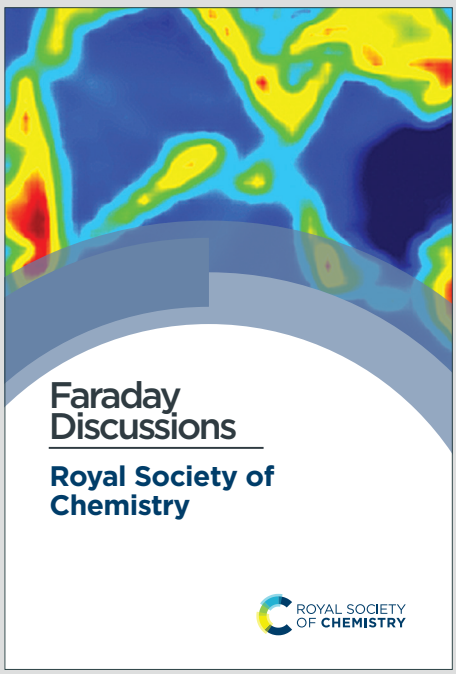

This article can be cited before page numbers have been issued, to do this please use: M. Nagarathinam, Y. Chen and O. V. Kolosov, *Faraday Discuss.*, 2026, DOI: 10.1039/D6FD00053C.

ROYAL SOCIETY OF CHEMISTRY

www.rsc.org/faraday_d

Atomic force nanorheology for *in-situ* exploration of nanoscale SEI layers in real-life rechargeable batteries electrodes.

View Article Online
DOI: 10.1039/D6FD00053C

[1]Mangayarkarasi Nagarathinam, [2]Yue Chen and [1]*Oleg Kolosov.

[1]Physics department, Lancaster University, Lancaster, UK
[2]College of Physics and Energy, Fujian Normal University Fuzhou 350117, PRC.

*o.kolosov@lancaster.ac.uk

Abstract.
Solid electrolyte interphase (SEI) is a nanoscale thin layer with complex nanomechanical properties that separates batteries negative electrode and the electrolyte to allow free flow of active ions (Li or Na), while precluding electron flow. Robust and high-performance SEI is critical for batteries performance, cyclability and safety, and the ability to study SEI properties in real-space and real-time (*operando*) holds the key for development of efficient and safe batteries. Here we report an efficient approach allowing to probe the nanoscale mechanical homogeneity of SEI layers with the nanoscale depth resolution via scanning nanorheology microscopy (NRM). In NRM the shear forces acting on the atomic force microscopy (AFM) nanoscale tip measured as tip penetrates the SEI layer from the electrolyte to the solid electrode surface provide a 1D quantitative measure of local storage and loss elastic moduli of the SEI along the path of the tip. A key feature of a new 1D-NRM is the ability to probe nanoscale SEI dynamics *operando* in real-life battery electrodes that have micrometre scale roughness while providing nanometre scale depth resolution. Significantly, we show that due to the nature of shear-force measurements, NRM effectively eliminates the dependence of the measurements on the diameter of the AFM tip, a parameter that otherwise the hardest to quantify in AFM nanomechanical measurements. We successfully apply a new approach to quantify details of SEI formation process on the hard carbon negative electrodes in Na-ion batteries.

1. Introduction.

If one were asked to single out the most critical component in the non-aqueous rechargeable batteries, including lithium-ion, sodium-ion and next generation emerging metal-based batteries it is likely to be a solid electrolyte interphase, or SEI[1]. In batteries, SEI is a few tens of nanometre thick passivation layer that forms at the negative electrode-liquid electrolyte interface during the initial chemical or electrochemical reduction of the electrolyte. At the initial cycling stage– often referred as “formation”, SEI growth results in irreversible capacity loss and hence a drop in coulombic efficiency. During storage and cycling operation, the battery components (positive and negative electrodes, electrolytes) further decompose, and the initially formed SEI evolves which eventually leads to capacity fade and power fade. As this dynamic character of SEI results in the continuous consumption of electrolyte and active metal ions from the system, SEI is one of the major contributor in ensuring both efficient battery operation over multiple cycles and battery degradation[1]. In a nutshell, SEI formation at electrode-electrolyte interface in rechargeable batteries is unavoidable. To extend battery life and performance, it is vital to develop a stable and thin initial SEI, which can effectively

provide transport of ions to the electrode while acting as an effective barrier for the electrons, thus preventing further electrolyte decomposition and interfacial restructuring.

View Article Online
DOI: 10.1039/D6FD00053C

The SEI is composed of organic and inorganic components of crystalline, amorphous and polymorphic phases as well as trapped gases, electrolytes and salts[2]. This mix results in complex nanomechanical properties of SEI ranging from a viscous solvent-like, soft outer region to a mixed organic and inorganic transition layer with moderate stiffness and stiff inorganic inner layer adjacent to the electrode. These properties evolve dynamically in *real-time* battery operating conditions and can be effectively described via the "viscoelastic", or rheological, concept, where storage elastic moduli (such as Young's and shear moduli) are coupled with the loss moduli, the viscous response associated with the flow of the material, such as in liquids[3-5]. The viscoelastic properties of SEI play an important role in accommodating volume expansion, in Li-ion batteries, suppressing lithium dendrite formation, with the compromised mechanical stability of interphases leading to the catastrophic failure in batteries[6]. These factors call for novel real-space nanoscale resolution methods for measurement of SEI physical proportion that match the nanoscale dimensions of SEI and its heterogeneous components. Significantly, such SEI evaluation has to be performed *in situ* with electrolyte in contact with the electrode and, more preferably, in real-time, or *operando,* conditions when the battery is being charged or discharged[7-9].

Current techniques for mapping of *real-space* and *real-time* properties of SEI include optical microscopy which lateral resolution is unavoidably limited by the micrometre scale of wavelengths of light. [10,11]. Scanning electron and transmission electron microscopies do provide required nanoscale spatial resolution, however, they require high vacuum and are therefore not compatible with liquid electrolytes used in typical batteries. Recent advances in operando TEM/STEM, particularly using liquid-cell configurations, have enabled direct visualization of interfacial evolution under electrochemical conditions and reflects structural, compositional and mass-thickness variations[12]. However, such approaches remain limited in probing nanomechanical properties. In contrast, atomic force microscopy (AFM) that is capable to measure local physicochemical properties, e.g. nanomechanical or electrical with nanoscale resolution provides an alternative approach that can overcome these limitations, enabling the direct space-nanoscale studies of SEI's under realistic electrochemical environment.

AFM is a scanning probe microscopy technique that employs the nanoscale sharp tip to map material surfaces via tip-surface force interaction, and it can be operated in the liquid and electrochemical environments. By providing the topographic images of the electrode surfaces, AFM has shown to effectively visualize the electrode degradation, metallic plating, and SEI growth[13-16]. By employing nanomechanical AFM modes such as force modulation (FM), quantitative nanomechanical mapping, QNM, force-volume (FV) [2,17-19] and ultrasonic force microscopy (UFM) modes[20-22], AFM can observe the changes of local mechanical moduli of relatively stiff regions such as inorganic components of the SEI directly on electrode surface. However, these nanomechanical AFM techniques are inherently more sensitive to elastic or moderately stiff materials, while mapping and quantifying nanomechanical properties of highly viscous or liquid-like regions of the SEI remain challenging due to dissipative and time-dependent response of such layers.

View Article Online
DOI: 10.1039/D6FD00053C

Recently, our group has demonstrated that it is possible to explore the whole thickness of nanoscale SEI from the outer viscous-like layer to inner stiff layers using the interactive measurement of the local shear moduli of the SEI on the model graphite surface as the nanoscale sharp AFM tip penetrates the SEI layer. This approach was called three-dimensional (3D) nano-rheology microscopy (3D-NRM) [23,24]. While 3D-NRM allows the construction of 3D maps of the SEI with the lateral resolution of ~20 nm and vertical resolution below ~5 nm, while simultaneously mapping local mechanical properties across the layered structure, these measurements were performed on an extremely simplified system of atomically flat graphite layers with the roughness of sub-nm scale. At the same time, all realistic electrodes in the batteries are not atomically flat materials and consist of sub to a few micrometres sized grains mixed with carbon black and polymeric binder resulting in the electrode roughness on the micrometre scale.

Here we present for the first time a modified NRM workflow that allows to evaluate with the nanometre scale depth resolution the viscoelastic properties real-life electrodes SEI. The key component of this new approach is dynamic referencing of the solid-solid point of contact between the probing tip and the electrode surface with nanometre scale precision at each measurement location. At each location consists of approximately 20x20 nm^2 area, multiple measurements in adjacent nanoscale-spaced areas provide quantitative measure of average values and their statistical spreading of elastic and viscous components of the SEI as a function of SEI height above the electrode surface. We call this methods 1D-NRM, and while it does not directly reconstruct full 3D image of the SEI, it does evaluate the lateral and vertical nanoscale inhomogeneity and nanomechanical properties of the SEI *operando* for any real-life micrometre scale rough electrodes on the ~20-50 nm lateral length scale and <5 nm vertical scale. In this paper, we outline the complete workflow of the 1D-NRM measurements, encompassing measurement setup, instrumental requirements, and data analysis and means for the efficient presentation of the resulting nanomechanical characterization. These results are supported by the finite elements analysis (FEA) of the AFM tip - SEI layer interaction, to quantitatively extract the nanomechanical rheological properties of the SEI layer. Finally, we demonstrate the application of the 1D-NRM for the *operando* measurements of SEI on the realistic rough hard-carbon (HC) electrodes in the Na-ion batteries half-cell configurations.

2. Why Nanorheology Microscopy (NRM) for SEI characterisation?

While multiple SPM techniques have been previously employed to probe the battery's interphase properties, they typically focused on the surface morphology of SEI[25]. At the same time, it is the nanomechanical properties that provide a more direct link to the local composition of SEI. The typical SEI is mechanically heterogeneous and not only composed of stiffer – crystalline inorganic components, but also of amorphous, soft and viscous organic and polymeric components that evolve continuously during cycling. Hence, there is a need of methodology which can capture these distinct nanomechanical regimes from viscous solvent-rich outer layer to dense inorganic inner layer (Fig. 1). The existing nanomechanical AFM modes described above generally probe the force interaction between the apex of AFM tip and the sample, making it difficult to probe the 3D structure of the SEI[2,17-22]. At the same time, NRM that measures the lateral forces acting on the side of the AFM tip as it penetrates the internal structure is fully suitable for these studies[24]. In NRM, sample is oscillated laterally at a few hundred Hz to a few kHz frequencies at a very small (nm to sub-nm) amplitude that does not disrupt the SEI due to the vibration. It is important to distinguish that while the

View Article Online
DOI: 10.1039/D6FD00053C

lateral oscillation amplitude is in nm range, the penetration depth is controlled independently through the normal approach of the tip, enabling stepwise probing of the SEI with nanometre scale resolution from the outer regions towards progressively stiffer domains. Also, rather than oscillating the tip and observing the damping of oscillation due to the tip-SEI interaction, NRM oscillates the sample leading to practically zero response outside of contact with the SEI obtaining the response that is directly proportional to the viscoelastic properties of the SEI. As the lateral response is not affected by the normal forces and is sufficiently large even for the relatively weak SEI gel components, NRM becomes directly suitable for studying the complex relatively soft viscoelastic structure of SEI layer including both soft, viscous and progressively stiffer inorganic components. Importantly, by tracking the evolution of the lateral force response as a function of penetration depth, NRM enables continuous mapping of the nanomechanical properties across the SEI, from the viscous solvent rich-outer layers to the denser mechanically stiff inorganic regions closer to the electrode surface. This capability is fundamentally distinct from electron microscopy techniques where contrast arises from mass-thickness variation rather than direct mechanical responses. For the purpose of studying the much stiffer inorganic component of SEI on the near surface of the electrodes or SEI-electrode interface, and the electrode itself, the UFM[22,26] would be a better choice, however this work is outside the scope of the present work.

3. Normal and shear force measurements in lateral modulation AFM.

AFM measures the forces acting between the apex of the nanoscale sharp tip positioned at the end of the flexible micromachined cantilever via its deflection. This deflection in modern AFMs is measured via either angular deflection of the laser beam reflected from the end of the cantilever or by the optical interferometry [27]. If only the normal forces F_n acting along the tip axis are present, the deflected laser beam lies in the same plane as the incident laser beam and the cantilever long axis. By calibrating the flexural spring constant of the cantilever, the tip-surface normal force is then directly found via cantilever deflection. With the typical cantilever spring constants, k_c, being in the range between 0.1 and 40 N m^{-1}, and the deflection sensitivity in the range of a few pm, the forces from a few pN to μN can be measured. The laser beam deflection angle, Φ, proportional to the tip normal displacement is typically detected as the voltage, V_n, so in order to link this to the tip displacement, the sample is brought in solid-solid contact with the tip and while the AFM sample is moved by the prescribed distance d_s with the piezo scanner, the ratio of this distance and the measured voltage V_n is recorded providing the absolute measurements of the tip deflection. By using a value of the spring constant of the cantilever, k_c, provided by the manufacturer, or calibrated via thermal tune or Sader method[28], the absolute value of the tip-surface normal force, F_n can be measured.

During AFM operation, the tip is scanned in a raster way across the surface using the three-axis piezo scanner to obtain the area image in x-y plane, while the normal force is kept constant using the feedback loop by changing/adjusting the vertical position of the sample, z_s, hence producing the topography image $z_s(x,y)$ of the sample with nanoscale lateral and vertical resolution. In addition to this normal interaction, the movement of the AFM tip across the sample surface also generates shear, also called lateral, forces. In a simple case, these forces are coming from solid-solid friction between the tip and the sample that can also be modified by the omnipresent in ambient conditions surface liquid layers. If the scanning direction is perpendicular to the long cantilever axis, the lateral force F_l creates the torque

View Article Online
DOI: 10.1039/D6FD00053C

$\tau = l_t F_t$, where l_t is the length of the cantilever tip, resulting in the torsion of the cantilever by the angle $\theta = \tau / k_t$ where k_t is the torsional stiffness of the cantilever. The magnitude of this torsion hence depends on the lateral force, tip length, and the torsional stiffness of the cantilever. The resulting torsion angle θ is detected by the out-of-plane (the plane defined by the incident laser beam and the cantilever long axis) deflection of the reflected laser beam using the quadrant light photodiode that registers voltage V_l. The lateral torsion angle of cantilever, θ, can be calibrated in a similar way as the normal response, by locking the tip in the solid-solid contact with the sample and moving it laterally with the AFM piezo scanner by prescribed value. The values of l_t and k_t can be directly derived from the geometrical parameters of the AFM cantilever-tip provided by the manufacturer, allowing then to directly evaluate lateral force as

$$F_l = \frac{\theta k_t}{l_t} \quad (1)$$

If the sample cannot be presented as a solid surface, such as in the case of a viscoelastic SEI layer with a thickness of several tens of nanometres, the situation changes dramatically. In this case, as the AFM tip penetrate into such a layer, additional forces emerge that act not only on the surface but also act along the side surface of the nanoscale tip, both along the parallel and perpendicular to the tip axis. As a result, the total lateral force, F_l acting on the AFM cantilever no longer solely represents only the surface interaction but corresponds to the integral contribution of the forces encountered by the individual layers of the SEI as the depth of penetration, z_p of the tip increases (Fig. 1 c). Here we assume that the penetration depth of tip into the SEI (typically < 100 nm) is at least two orders of magnitude smaller than the length of the tip (10-20 μm), allowing to consider that all lateral force is effectively applied to the apex region of the tip. However, despite this geometrical confinement, the measured lateral force F_l (z_p) does not purely represent a local interaction. Instead, as the tip penetrates into the SEI, it remains in contact with all the overlying layers it penetrated through. Therefore, the lateral force corresponds to the cumulative contribution of the material from the SEI surface down to the penetration depth, z_p (Fig. 1c). As a result, the direct measurement of F_l (z_p) provides the integrated force values down to the specific depth within the SEI. Then, by differentiating the F_l with respect to z_p (dF_l/dz_p), a quantitative parameter proportional to the rheological parameters of the individual layer at the specific penetration depth z_p can be obtained (Fig. 1d). In NRM the sample is oscillated in the lateral direction in x-y plane at the frequency f with the amplitude A_l, to generate time-dependent lateral displacement $d_l(t) = A_l \cos(2\pi f t)$, inducing a resulting lateral force response.

For viscoelastic materials such as the SEI, the response is phase shifted relative to the applied displacement and therefore represented as a complex quantity F^*_l, which includes both the in-phase (elastic) and out-of-phase (viscous) components. As mentioned earlier, depth-resolved derivative of this complex force (dF^*_l/dz_p), provides the local force response associated with the material at depth z_p proportional to the amplitude of the applied oscillation. To calculate the material response that is independent of the excitation conditions, the depth-resolved derivative is then normalized by the oscillation amplitude A_l that can be represented as a complex value - lateral sample compliance, $S^*(z_p)$ of the layer at the depth z_p,

$$S^*(z_p) = \frac{1}{A_l} \frac{dF^*_l}{dz_p} \quad (2)$$

View Article Online
DOI: 10.1039/D6FD00053C

This parameter represents the local viscoelastic response of the SEI per unit lateral displacement, effectively characterizing the depth-resolved shear stiffness of the materials. It is to be noted here that units of $S^*(z_p)$ are Nm^{-2}, the same units as the Young's elastic modulus, *E*, of the material. Clearly the force response should be proportional to the complex shear modulus of the SEI at the particular depth, $Y(z_p)$

$$E^*(z_p) \sim \frac{1}{A_l} \frac{dF^*_l}{dz_p} \quad (3)$$

One can use the reference materials with known elastic moduli or a finite element analysis (FEA) modelling to find the dimensionless coefficient of proportionality in Eq. 3 and hence quantify the complex shear modulus of the SEI at the particular depth, $Y(z_p)$. The complex elastic modulus $E^*(z_p)$ that correspond to the viscoelastic property of material can be decomposed into the real part $\mathrm{Re}[E^*(z_p)]$, which corresponds to the elastic (storage) component of elastic moduli, whereas the imaginary part $\mathrm{Im}[E^*(z_p)]$ reflects the viscous (flow component) behaviour of the SEI. The pathway for the quantification of elastic moduli is described in the next section.

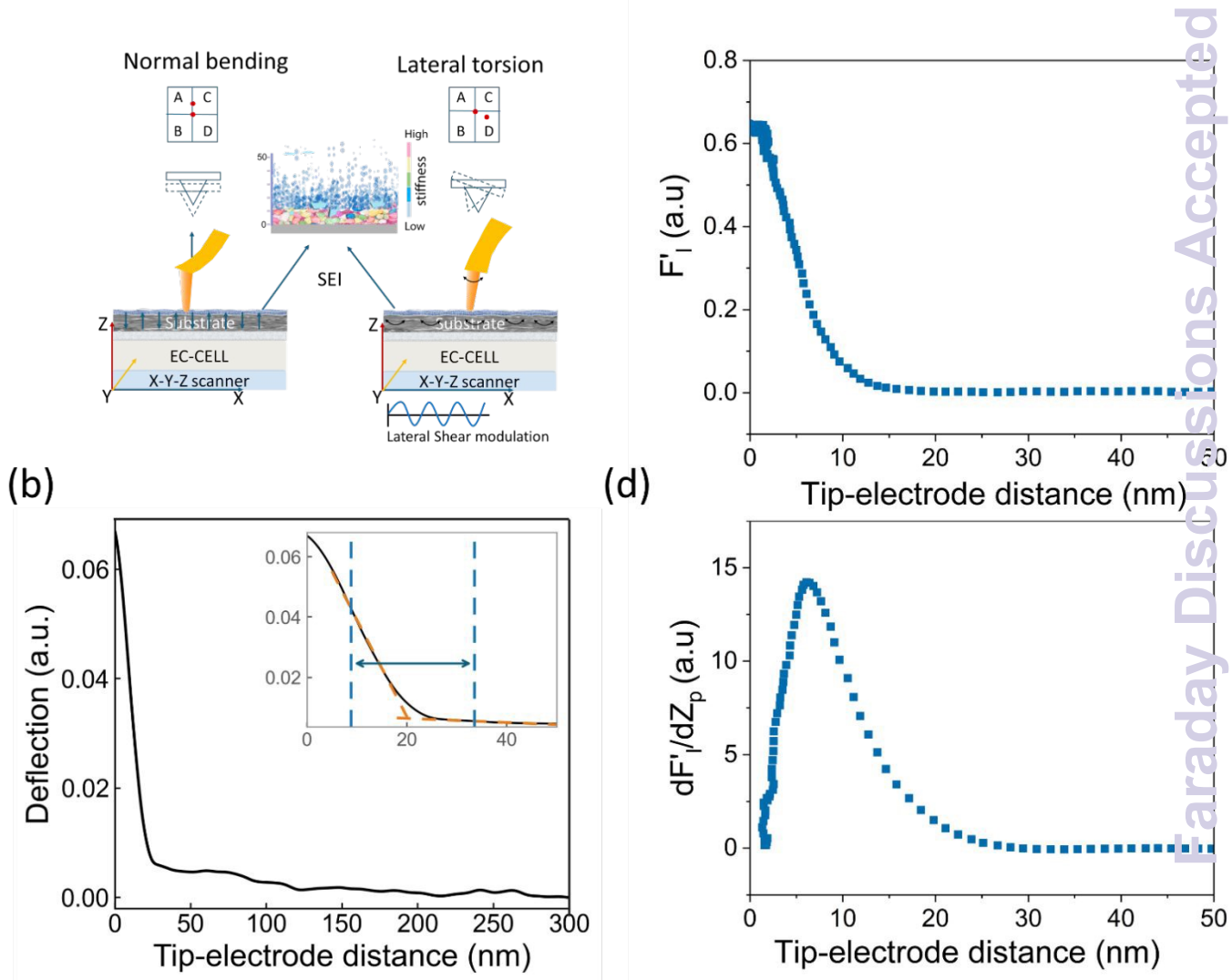

Figure 1. a) Schematics of normal and lateral forces acting on the AFM tip and cantilever, b) tip deflection vs sample displacement (experimental example), c) lateral force amplitude Re(F_l), d) derivative of d Re(F_t)/dz, inset – illustration of the multiphase SEI layer.

View Article Online
DOI: 10.1039/D6FD00053C

4. Quantification of the shear rheological properties of layers via NRM.

Here the step-by-step measurement methodology described in section 3 is employed to obtain the calibrated values of in phase and out of phase lateral forces acting on the tip, F_l^*, as a function of the tip penetration depth z_p,. During these measurements, it is assumed that the sample is laterally dithered with the amplitude A_l producing the time-dependent lateral displacement of the sample of $d_l(t) = A_l\cos(2\pi f t)$ perpendicular to the long axis of the cantilever. Since the viscoelastic response of the material is determined from the phase difference between the applied displacement and measured force, it is essential to ensure that this phase shift originates solely form the sample and not influenced by instrumental artefacts. In reality, the AFM scanner and actuator can introduce additional phase shifts, particularly near their resonance frequencies. For practical implementation it is therefore important to avoid the instrumental phase difference arise from actuator resonance. For example, if the sample scanning AFM scanner (Multimode, Bruker) is used, these resonances would typically be in the range of few Hz to a couple of kHz. Even if the shear transducers (e.g. from PI ceramics) are used, for the sample scanning AFMs used in our setup, the scanner is still expected to produce unwanted resonances. At the same time, the tip scanned AFMs (such as Bruker ICON or Park NX-10) would not have the same limitations and the dithering frequencies up to multiple tens of kHz can be used provided the sample itself is of a small mass. We also found that the amplitude of 0.5 to 2 nm of lateral dithering is more than sufficient for the effective mapping of the nanorheology of materials and provides sufficient sensitivity while maintaining a stable phase response and operation within the linear regime. Finally, the linear ("diving board") cantilevers with relatively small spring constant (from 0.1 to 3 Nm^{-1}) are the best for the NRM measurements due to the suitable torsional spring constant.

Once reliable experimental conditions and quantified lateral forces are measured, it is necessary to relate the measured lateral force response, F^*_l to the intrinsic mechanical properties of the material. Since the NRM signal is based on the lateral force acting on the tip, a physical description of how this force depends on the material properties, tip geometry and penetration depth is required. Here we use FEA to estimate the additional geometrical coefficient at the local deformation level to account for the nonuniform strain distribution in the SEI near the apex area of the tip.

Firstly, let's estimate the forces acting on the tip of radius r_t of which the length z_l is embedded in the uniform viscoelastic layer. Here we will approximate the AFM tip as the cylinder with radius r_t that given a typically small angle of the Si based AFM tips we used is a reasonable approximation, that can be further rectified if higher accuracy is required. The area of the intersection of the tip and the layer perpendicular to the tip motion is then $2r_tz_l$. Given that the amplitude of the normal displacement of the sample A_l (~1nm) is much smaller than the radius of the tip (~10 nm), the resulting strain due to the lateral movement of the tip with respect to the sample, can be estimated (subject to the dimensionless geometrical coefficient r_g) as $\gamma = r_g\frac{A_l}{r_t}\cos(2\pi f t)$ leading to the average stress $\sigma^* = E^*\gamma$, where E^* is the Young's modulus of the material. Then the average lateral force acting on the tip is the sum of the normal forces acting on the front and the back of the tip

$$F_l{}^* = 2\,E^*2r_tz_l\gamma = 4\,r_gE^*r_tz_l\frac{A_l}{r_t}\cos(2\pi f t) = 4\,r_gE^*A_lz_l\cos(2\pi f t) \quad (4)$$

View Article Online
DOI: 10.1039/D6FD00053C

Significantly, Eq. 4 shows that the dependence of the lateral force on the tip radius is fully eliminated, since the dependences of strain being inversely proportional to the tip radius while the area of contact experiencing the strain and hence the force is directly proportional to the tip radius. As the tip penetrates into the layer, the increment of the force(note that z_l=-z_p), $\frac{dF_l^*(z_p)}{dz_p}$ is proportional to the Young's modulus at the depth z_p allowing the extraction of the effective Young's modulus of the layer as

$$E^*(z_p) = \frac{1}{4\, r_g A_l} \frac{dF_l^*(z_p)}{dz_p} \quad (5)$$

The complex amplitude of the oscillating force can be expressed as $F_l^*(z_p) = F_l'(z_p) + iF_l''(z_p)$ where $F_l'(z_p)$ and $F_l'(z_p)$ represent the in-phase and out-of-phase components, respectively. By recording the real (in-phase) and imaginary (out-of-phase) components of the force $F^*_l(z_p)$ as the AFM tip penetrates the SEI using lock-in amplifier (SRS830, Stanford research instruments) and then differentiating with respect to z_p, the storage *E'* and loss *E''* moduli (where *E*=E'+iE"*) of the SEI material at the depth z_p can be directly obtained.

Finally, as for the soft materials (gel-like, rubber etc) that can be with good approximation considered as non-compressible media, the Poisson's ratio, ν, becomes close to 0.5. In this case the shear modulus becomes

$$G^*(z_p) = \frac{E^*(z_p)}{2(1+\nu)} \approx \frac{1}{3}E^*(z_p) \quad (6)$$

We then can link the real and imaginary part of measured $G^* = G' + iG''$with position variable viscosity determined as

$$\eta(z_p) = \frac{G''(z_p)}{2\pi f} = \frac{E''(z_p)}{6\pi f} \quad (7)$$

The dimensionless coefficient r_g is found as below using the finite elements analysis (FEA) simulation by comparison of the simulated dependence $\frac{dF_{lt}^*(z_p)}{dz_p}$ for the homogeneous layer of reference material with known Young's modulus E_{ref} under known amplitude of the lateral sample vs tip motion. In this case the r_g is found as

$$r_g = \frac{1}{4\, A_l E_{ref}} \frac{dF_l^*(z_p)}{dz_p} \quad (5)$$

We compared the obtained values of E^* and $\frac{1}{4A_l E_{ref}} \frac{dF^*_l}{dz_p}$ to obtain r_g for the cylindrical tip. Fig. 2 shows the results of the simulation, showing the 3D and cross-section views of displacement and stress and the calculated force vs penetration (Fig 2c) that allows to calculate the coefficient of r_g for 2 nm lateral excitation amplitude A_l, 1 kHz oscillation frequency, and 1 MPa and 3 MPa Young's moduli layer, as $r_g = \frac{1}{4\times 2\text{ nm}\times 1\text{ MPa}} \frac{1\text{ nN}}{100\text{ nm}} \approx 1.25$.

Notably, using exact simulations, we find that r_g is close to 1, validating our empirical estimates of the forces in the beginning of this section, and significantly, that the 1D-NRM does not require the exact knowledge of the tip diameter, that in other nanomechanical modes, one of the most difficult experimental parameters to quantify, and that directly influences the quantitative measurements in other, non-NRM nanomechanical modes[2,17-22].

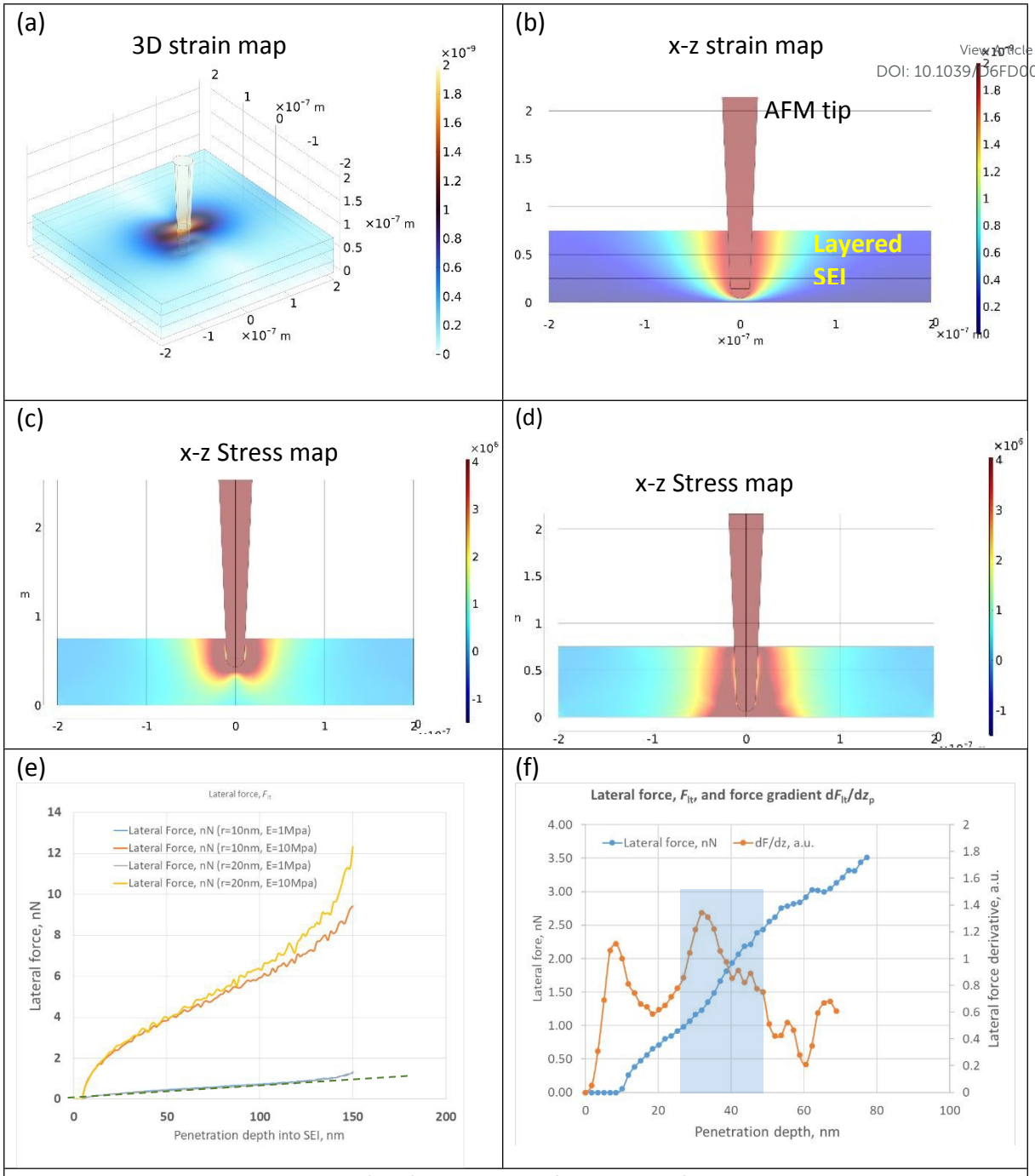

Figure 2. Finite elements analysis (FEA) simulation of the lateral force in the NRM tip penetrating the SEI model layer. a) 3D and b) cross-plane view of the amplitude of the displacement of the SEI layer, c) and d) cross-sectional maps of the stress in the measured layer at different penetration depth (tip radius 10 nm). e) Graphs of the lateral force for two layers with 1 MPa and 10 MPa Young's moduli and tip radii of 10 and 20 nm as a function of the penetration depth; significantly, the response of NRM practically does not depend on the tip diameter making quantitative NRM approach possible without knowledge of the exact diameter of the AFM tip; the linear part of the penetration curve of 1 MPa layer is used to find the dimensionless coefficient r_g=1.25, that is necessary for the quantitative measurements of the Young's and hence shear moduli of the SEI as the function of the depth; the deviation from the linearity is expected as the tip-surface distances becomes comparable with the tip radius of 10 nm. f) Simulation of the force and force derivative profile for the SEI structure with the internal stiff ("skin") layer marked as blue rectangle. The derivative of the force reliably picks up the inhomogeneity in the SEI internal nanostructure.

DOI: 10.1039/D6FD00053C

5. *Operando* mapping of the SEI growth in the Na-ion system with real-life hard carbon electrodes.

The previous reports of 3D-NRM approach in understanding nanomechanical properties were using model electrodes, such as highly oriented pyrolytic graphite (HOPG) with atomic scale flatness with minimal surface roughness. Under these conditions, the electrode surface can be treated as a well-defined global reference, and this enables direct evaluation of the viscoelastic properties of the SEI in nanometre scale spatial resolution. However, in real battery electrodes, such as hard carbon, exhibit complex and heterogenous surface morphologies, with particle sizes ranging from hundreds of nanometres to micrometres, resulting in surface roughness which is 10 s / 100 s of magnitude larger than that of model electrodes (Fig. 3 a-b). For example, the variation in morphology and surface roughness leads to difference in measurements ie at point A, the surface is ~0 nm and point B, the surface is ~500 nm. Under such conditions, conventional global depth-referenced measurements become unreliable, as variations in topography obscure the true position of the electrode surface.

To address this limitation, here we focus on the ability to exactly pinpoint the position of the surface of the electrode and reference all nanorheological measurement to this point (Fig. 3e). Using this approach, multiple measurements were acquired over large area (few hundreds nm to µm) with the lateral spacing in the order of nanometre scale steps (~50-100 nm) in a single statistical pool. Each measurement is locally referenced to the electrode surface by defining the solid-solid contact as zero tip-surface distance even when the adjacent points can have micrometre scale height difference. In order to do that we considered that for the sample far from the tip, the normal force F_n vs sample position, d_s>>0, dependence $F_n(d_s)$=0 hence flat, a there is no normal force acting on the tip. At the same time, once the tip touches the sample and therefore the sample pushes the cantilever up with d_s<<0, in the limit of the high tip-surface force, the solid-solid contact is established and, in the tip, follows the sample surface providing linear dependence of $F_n(d_s)$. The intersection of these two lines – at the d_s>>0 and d_s<< 0 is therefore used as a point of the solid-solid contact and is independent on the layers above the solid electrode surface. This procedure is automatically applied to each local measurements allowing to reliably provide the ensemble of measurements referenced to the sample surface with nanometre scale accuracy, even when the roughness of the sample is several orders of magnitude higher at the micrometre scale.

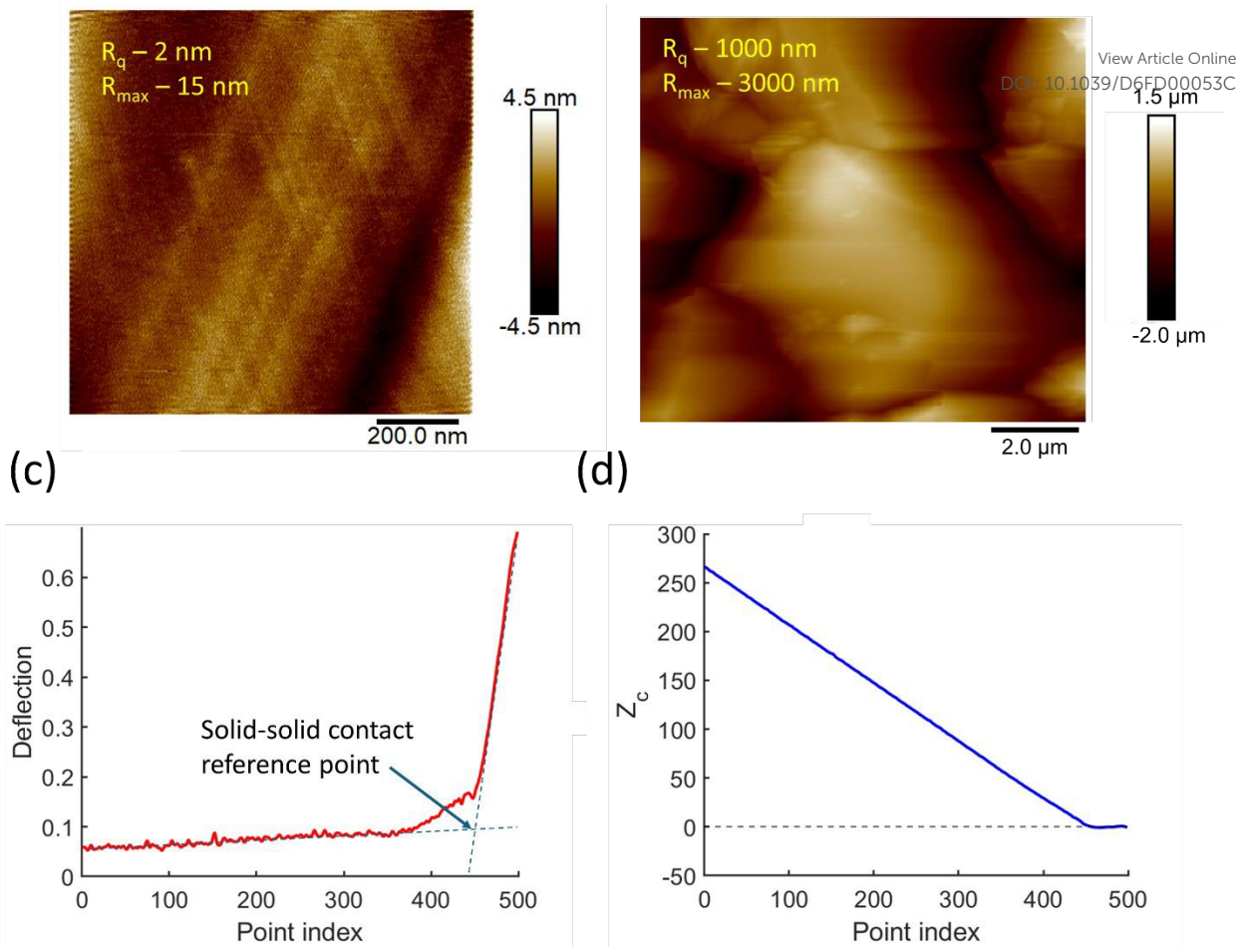

Figure 3. a) HOPG and b) HC negative electrode and their roughness values, c) raw data of the deflection vs sample displacement (measured in increments points) for the sample in b) obtained in the measurement, in arbitrary units, the intersection of the base line and high force solid-solid contact line defines the solid-solid contact point, d) processed data with calibrated tip-electrode surface distance from the (calibrated vertical sale in nm), with solid-solid contact as origin as a function of the same increment steps.

View Article Online
DOI: 10.1039/D6FD00053C

The core of this approach is shown in panels (Fig. 3c,d) where the normal force displacement behaviour is used to determine the point of solid-solid contact for each individual measurement. When the tip is far from the electrode surface, ie., in the non-contact regime the normal force remains negligible whereas upon contact, the cantilever deflection increases linearly with sample displacement. The intersection of this regime defines the contact point and assigned as zero tip-surface distance (z_p = 0) as shown in Fig. 3c. This procedure is applied independently to each measurement location, which enable accurate reference of depth coordinates across regions with large topographical variation as in Fig. 3b. By referencing all measurements to the locally determined surface position, this method enables the acquisition of statistically meaningful, depth-resolved nano rheological data across large areas of rough electrodes. The resulting aligned datasets form the basic data set for subsequent analysis including depth-dependent viscoelastic nanomechanical profiling and statistical evaluation of the SEI heterogeneity.

To probe SEI formation on real hard carbon electrodes (HC) with high surface roughness, *operando* EC-NRM measurements were performed on HC vs Na system during initial sodiation using cyclic voltammetry from open circuit voltage (OCV) to 0.005 V vs Na/Na^+ in 1.0 M $NaPF_6$ in EC:DEC (1:1 v/v) at 1.0 mV s^{-1} (Fig. 4a). The depth resolved lateral force (dF_l/dz_p), extracted from the local referencing approach is shown in Fig. 4b. The voltage range was divided into distinct regions corresponding to different stages of electrolyte reduction and SEI formation. The solid lines represent the mean profiles obtained by averaging all individual curves measured at each location in the voltage regions. While the shaded regions represent the 95% confidence interval of the mean, reflecting the statistical uncertainty of the ensemble-average response. The averaged profiles illustrate the variation of the local shear response as a function of the tip-surface distance z_p. From Fig. 4b, it's well understood that at large z_p, ie when the tip is away from the electrode surface, no lateral shear response is detected. As the tip approaches the surface, it begins to interact with the outer regions of the SEI and the measured response increases progressively with decreasing tip-surface distance. This increase reflects the gradual engagement of the probe with the interphase as it penetrates across the SEI from the outer soft organic to the inner stiff regions and provides an integrated measure of the SEI thickness across different electrochemical states.

For hard carbon electrodes, the onset and evolution of the response vary with the voltage regions (Fig. 4b). However, a pronounced response is observed within the first few nanometres from the surface, followed by a gradual decay with increasing distance from the electrode surface across all voltage regions. At higher potentials (1.5-2.0 V), the response is weak at the far regions and confined to the near-surface region and indicate the absence of a well-developed interphase. As the potential decreases to 1.0-1.5 V, the onset of the interaction is below 15 nm and gradually increases to ~2 nm and drops down and indicated the development restructuring of the SEI. At 0.5-1.0 V region, the onset of the interaction shifts to larger distances, suggesting the formation of a progressively thicker SEI. The gradual increase in lateral force response, reflects the formation of soft skin-like or mechanically compliant outer regions and transition towards denser or stiffer domains closer to the electrode surface *i.e.*, below 5nm. However, at the very low potential region 0.005-0.5 V, the onset of interaction begins at even at larger distance (20-30 nm) and the stiffness near the electrode surface decreases that indicates the formation of thicker and stable heterogeneous

View Article Online
DOI: 10.1039/D6FD00053C

SEI. The response on hard carbon is distributed over a broad range compared to the well-defined peaks which indicate sharp transitions between layers in model flat systems. The observation of high NRM response near the electrode surface (0-5 nm) indicates the presence of mechanically stiffer SEI domains and mixed response at the intermediate depths (5-10 nm).

The two-dimensional kernel density (2D-KDE) maps[29] of the absolute value of complex shear modulus $|G^*(z_p)|$ as a function of tip-penetration distance z_p, further illustrate the spatial distribution of the mechanically distinct SEI domains, (Fig. 4c). The KDE maps represent the continuous probability density in $|G^*_{(zp)}|$ in z_p space, where darker regions correspond to higher population density. These maps reveal distinct mechanical populations across voltage. At higher voltage region, the KDE is concentrated near low response values and shallow depths indicating mixed and limited interphase development. As the potential decreases, the distribution broadens both in response and depth, reflecting the emergence of heterogeneous SEI components. At low voltage regions, the KDE exhibits a pronounced spread with contributions at higher response and SEI thickness, consistent with the formation of a thicker and structurally complex interphase.

The depth dependent viscoelastic response and their redistribution is further quantified using "violin plots" across the depth intervals (0-5 nm, 5-10 nm, 10-20 nm). In these plots, the width of the violin at a given value reflects the probability density of the data, ie., wider regions corresponding to a higher concentration of the measurements. At higher voltage regions (1.5-2.0 V, at outer SEI (5-10 and 10-20 nm), the distributions exhibit clear multimodal features reflecting the heterogeneous nature of hard carbon surface and the presence of varying local environments. However, at near-surface region (0-5 nm), violin remains relatively narrow and predominantly uniform indicating limited interphase development and a response largely related to the underlying electrode. At intermediate potentials (0.5-1.0 V), the response becomes more pronounced at all depth regions. Especially, at 0-5 nm, the distribution shifts towards higher response values indicating the formation of a inner SEI. At 5-10 nm, the violin plots broaden significantly and begin to exhibit multimodality. This suggests the coexistence of multiple mechanical populations associated with transitioning interphase. At 10-20 nm, the violin plot reveals the development of a more extended outer SEI layer. At the low voltage region (0.005-0.5 V), shows a higher response value at 0-5 nm is consistent with a mechanically robust inner SEI. At intermediate depths, distinct multiple peaks are observed indicating the presence of overlapping mechanical domains. In the outer SEI region (10-20 nm), the widespread and increased population reflect the formation of a thick heterogenous outer SEI composed of softer and more compliant components.

Overall, Fig. 4 demonstrates that the 1D-NRM approach enables reliable, depth-resolved and statistically robust characterization of SEI nano mechanics on realistic hard carbon electrodes. The combined use of mean profiles, KDE maps and violin plots reveals not only the evolution of a viscoelastic response with voltage, but also the emergence and redistribution of heterogeneous nanomechanical populations across depth. These results confirm that the method effectively decouples nanoscale interphase properties from microscale surface roughness and provides comprehensive framework to probe complex electrochemical interphases in operando.

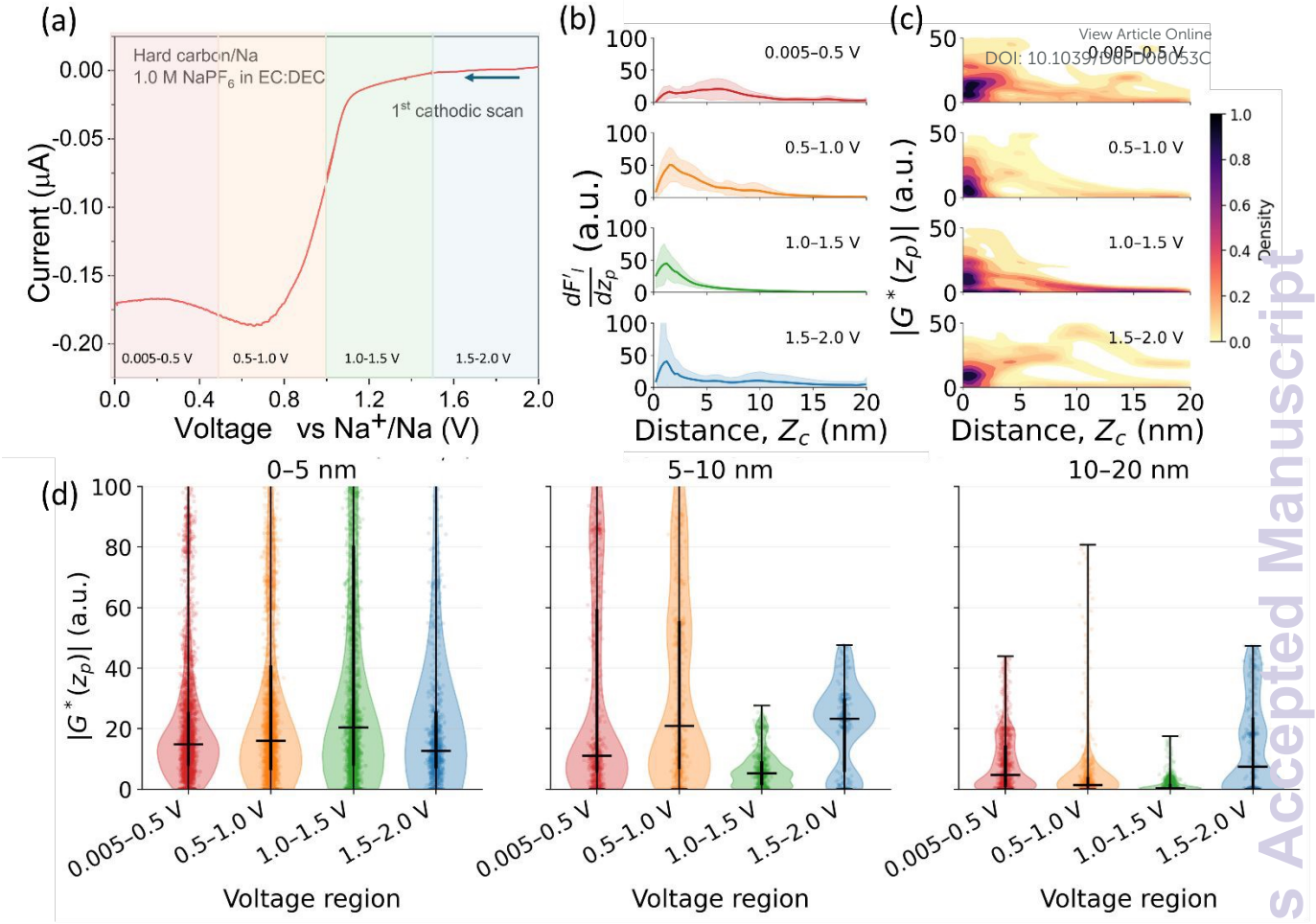

Figure 4. Operando 1D-NRM analysis of SEI evolution on hard carbon /Na system in 1.0 M $NaPF_6$ in EC:DEC a) 1st cathodic or sodiation profile obtained from cyclic voltammetry at 1 mV s^{-1} highlighting the voltage regions used for further analysis b) Depth resolved Re (dF'_l/dz_p) profiles showing the evolution of elastic response (mean ±Cl), c) Kernel density estimation (KDE) maps of the magnitude of complex shear response $|G^*(z_p)|$ as a function of depth and voltage and d) Violin-plots of $|G^*(z_p)|$ distributions for 0-5 nm, 5-10 nm and 10-20 nm respectively.

The observed evolution of depth-dependent nanomechanical response in real battery electrodes with rough surface through NRM is broadly consistent with the reports on SEI formation in sodium-ion systems which describe an initial formation of an organic-rich outer SEI and an inorganic-rich inner layer based on compositional depth profiling such as Hard X-ray photoelectron Spectroscopy (HAXPES) and Time-of-Flight Secondary Ion Mass spectrometry (ToF-SIMS[30]). This aligns with the transition from initial electrolyte assisted decomposition to the formation of an extended, organic-rich outer SEI and a denser inorganic-rich inner layer. However, NRM measurements directly resolve the spatial distribution and dynamic redistribution of these mechanically distinct domains across depth revealing the inherent heterogeneity of the SEI. This heterogeneity remains typically obscured in conventional measurements where the response reflects the mass-thickness variations integrated along the measurement direction ie., effectively averaging contributions from multiple depths.

View Article Online
DOI: 10.1039/D6FD00053C

Conclusions.

Here we report a novel approach based on AFM and the nanorheology microscopy (NRM) principle, allowing to probe the nanoscale mechanical properties of nanoscale SEI layers of real-life battery electrodes that have the micrometre-scale roughness. We demonstrate that the NRM response is largely independent of the AFM tip radius within a reasonable range, therefore eliminating one of the most difficult parameters in the nanomechanical studies via AFM and allowing the true quantification of the nanorheological properties of the SEI with nm scale depth resolution. By referencing the force-distance maps to the solid-solid-solid contact we can observe the dynamic of the SEI growth on the hard carbon negative electrodes in the half-cell Na- ion batteries under *operando* while providing a few nanometres depth resolution. Furthermore, by probing the areas with approximately 50 nm lateral step size we achieve high quality informative statistical analysis of both vertical and lateral variability of these electrodes.

Acknowledgements.

The authors are grateful to the Faraday Institution NEXGENNA project (FIRG018), UKRI support via strategic capital equipment grant HiWiN (EP/V00767X/1) to OVK, Bruker Ltd for the technical expertise and support, Faradion for providing the electrode materials samples, Fushou University for the Visiting Professorship to OVK, and EU ERC grant TheMA supporting the new development of the nanoscale methodologies (101117958).

References.

1 Bommier, C. & Ji, X. Electrolytes, SEI Formation, and Binders: A Review of Nonelectrode Factors for Sodium-Ion Battery Anodes. *Small* **14** (2018). https://doi.org/10.1002/smll.201703576

2 Zhang, Z. *et al.* Capturing the swelling of solid-electrolyte interphase in lithium metal batteries. *Science* **375**, 66-70 (2022). https://doi.org/doi:10.1126/science.abi8703

3 Benaglia, S., Amo, C. A. & Garcia, R. Fast, quantitative and high resolution mapping of viscoelastic properties with bimodal AFM. *Nanoscale* **11**, 15289-15297 (2019). https://doi.org/10.1039/c9nr04396a

4 Attard, P. Measurement and interpretation of elastic and viscoelastic properties with the atomic force microscope. *Journal of Physics-Condensed Matter* **19** (2007). https://doi.org/10.1088/0953-8984/19/47/473201

5 Rother, J., Noding, H., Mey, I. & Janshoff, A. Atomic force microscopy-based microrheology reveals significant differences in the viscoelastic response between malign and benign cell lines. *Open Biology* **4** (2014). https://doi.org/10.1098/rsob.140046

6 Cheng, X.-B., Zhang, R., Zhao, C.-Z. & Zhang, Q. Toward Safe Lithium Metal Anode in Rechargeable Batteries: A Review. *Chem. Rev.* **117**, 10403-10473 (2017). https://doi.org/10.1021/acs.chemrev.7b00115

7 Li, Y. *et al.* Atomic structure of sensitive battery materials and interfaces revealed by cryo–electron microscopy. *Science* **358**, 506-510 (2017). https://doi.org/10.1126/science.aam6014

8 Huang, W. *et al.* Evolution of the Solid–Electrolyte Interphase on Carbonaceous Anodes Visualized by Atomic-Resolution Cryogenic Electron Microscopy. *Nano letters* **19**, 5140-5148 (2019). https://doi.org/10.1021/acs.nanolett.9b01515

9 Xu, Y. *et al.* Atomic to Nanoscale Origin of Vinylene Carbonate Enhanced Cycling Stability of Lithium Metal Anode Revealed by Cryo-Transmission Electron Microscopy. *Nano letters* **20**, 418-425 (2019). https://doi.org/10.1021/acs.nanolett.9b04111

10 Li, C.-Y. *et al.* Unconventional interfacial water structure of highly concentrated aqueous electrolytes at negative electrode polarizations. *Nature communications* **13** (2022). https://doi.org/10.1038/s41467-022-33129-8

11 Zhang, W. *et al.* Engineering a passivating electric double layer for high performance lithium metal batteries. *Nature communications* **13**, 2029 (2022). https://doi.org/10.1038/s41467-022-29761-z

12 Hu, H., Yang, R. & Zeng, Z. Advances in Electrochemical Liquid-Phase Transmission Electron Microscopy for Visualizing Rechargeable Battery Reactions. *ACS Nano* **18**, 12598-12609 (2024). https://doi.org/10.1021/acsnano.4c03319

13 Liu, T. *et al.* In situ quantification of interphasial chemistry in Li-ion battery. *Nature nanotechnology* **14**, 50-56 (2019). https://doi.org/10.1038/s41565-018-0284-y

14 Liu, X. R., Wang, L., Wan, L. J. & Wang, D. In situ observation of electrolyte-concentration-dependent solid electrolyte interphase on graphite in dimethyl sulfoxide. *ACS Appl Mater Interfaces* **7**, 9573-9580 (2015). https://doi.org/10.1021/acsami.5b01024

15 Shi, Y., Yan, H.-J., Wen, R. & Wan, L.-J. Direct Visualization of Nucleation and Growth Processes of Solid Electrolyte Interphase Film Using in Situ Atomic Force Microscopy. *ACS Applied Materials & Interfaces* **9**, 22063-22067 (2017). https://doi.org/10.1021/acsami.7b05613

16 Zhang, Z. *et al.* Characterizing Batteries by In Situ Electrochemical Atomic Force Microscopy: A Critical Review. *Adv. Energy Mater.* **11**, 2101518 (2021). https://doi.org/https://doi.org/10.1002/aenm.202101518

17 Gao, Y. *et al.* Unraveling the mechanical origin of stable solid electrolyte interphase. *Joule* **5**, 1860-1872 (2021). https://doi.org/https://doi.org/10.1016/j.joule.2021.05.015

18 Zheng, J. *et al.* 3D visualization of inhomogeneous multi-layered structure and Young's modulus of the solid electrolyte interphase (SEI) on silicon anodes for lithium ion batteries. *Physical Chemistry Chemical Physics* **16**, 13229-13238 (2014). https://doi.org/10.1039/C4CP01968G

19 Gu, Y. *et al.* Designable ultra-smooth ultra-thin solid-electrolyte interphases of three alkali metal anodes. *Nature communications* **9**, 1339 (2018). https://doi.org/10.1038/s41467-018-03466-8

20 Grier, E. J. *et al.* Structural changes to epitaxial (0001) holmium layers during hydrogen loading. *Journal of Physics D-Applied Physics* **33**, 894-900 (2000). https://doi.org/10.1088/0022-3727/33/8/302

21 Bosse, J. L., Tovee, P. D., Huey, B. D. & Kolosov, O. V. Physical mechanisms of megahertz vibrations and nonlinear detection in ultrasonic force and related microscopies. *Journal of Applied Physics* **115** (2014). https://doi.org/10.1063/1.4871077

22 Chen, Y. *et al.* Hidden subsurface molecular bubbles in graphite anodes for LIBs. *Energy & Environmental Science* **18**, 8430-8445 (2025). https://doi.org/10.1039/D5EE01076D

23 Chen, Y. *et al.* Operando nano-mapping of sodium-diglyme co-intercalation and SEI formation in sodium ion batteries' graphene anodes. *Applied Physics Reviews* **11** (2024). https://doi.org/10.1063/5.0196568

24 Chen, Y. *et al.* Nanoarchitecture factors of solid electrolyte interphase formation via 3D nano-rheology microscopy and surface force-distance spectroscopy. *Nature Communications* **14**, 1321 (2023). https://doi.org/10.1038/s41467-023-37033-7

25 Zhang, Z. *et al.* Operando Electrochemical Atomic Force Microscopy of Solid–Electrolyte Interphase Formation on Graphite Anodes: The Evolution of SEI Morphology and Mechanical Properties. *ACS Applied Materials & Interfaces* **12**, 35132-35141 (2020). https://doi.org/10.1021/acsami.0c11190

26 Tinker-Mill, C., Mayes, J., Allsop, D. & Kolosov, O. Ultrasonic force microscopy for nanomechanical characterization of early and late-stage amyloid-ß peptide aggregation. *Sci Rep* **4** (2014).

27 Miyahara, Y. *et al.* Optical excitation of atomic force microscopy cantilever for accurate spectroscopic measurements. *EPJ Techniques and Instrumentation* **7**, 2 (2020). https://doi.org/10.1140/epjti/s40485-020-0053-9

28 Sader, J. E. *et al.* Spring constant calibration of atomic force microscope cantilevers of arbitrary shape. *Review of Scientific Instruments* **83** (2012). https://doi.org/10.1063/1.4757398

29 King, T. L., Bentley, R. J., Thornton, L. E. & Kavanagh, A. M. Using kernel density estimation to understand the influence of neighbourhood destinations on BMI. *BMJ Open* **6**, e008878 (2016). https://doi.org/10.1136/bmjopen-2015-008878

30 Fitzpatrick, J. R. *et al.* An in-depth Study of the Solid Electrolyte Interphase Compositional Evolution in Sodium-Ion Batteries: Unravelling the Effects of a Na Metal Counter Electrode on the SEI. *Advanced Science* **12**, e04717 (2025). https://doi.org/https://doi.org/10.1002/advs.202504717

View Article Online
DOI: 10.1039/D6FD00053C

The authors have all experimental data available on the readers' request.

View Article Online
DOI: 10.1039/D6FD00053C

On behalf of all authors,
Oleg Kolosov.

Physics department, Lancaster University, Lancaster, UK
*o.kolosov@lancaster.ac.uk